E-Combretastatins as anti-cancer prodrugs activated by photoisomerization

Contact *r.h.bisby@salford.ac.uk*

K.M.Scherer
Biomedical Science Research Centre, University of Salford Salford M5 4WT, UK

R.H.Bisby
Biomedical Science Research Centre, University of Salford Salford M5 4WT, UK

A.W.Parker
STFC Lasers for Science Facility, Research Complex at Harwell, OX11 0FA

S.W.Botchway
STFC Lasers for Science Facility, Research Complex at Harwell, OX11 0FA

Introduction

Combretastatin A4 (as the *Z*-(*cis*)isomer) is a well investigated anticancer agent that inhibits microtubule assembly, induces apoptosis in target vascular cells and prevents tumour growth by inhibiting development of new blood vessels [1,2]. The corresponding *E*-(*trans*) isomer is less active by about 2 orders of magnitude [3] and therefore might function as a prodrug, activated by photochemical isomerisation. Although *E*-combretastatins absorb in the ultraviolet (300-360 nm), we have shown that the fluorescent state, from which photoisomerization occurs, may also be populated by two-photon absorption in the region of 630 nm [4]. At these longer wavelengths enhanced light penetration into tissues makes controlled photophysical drug activation *in situ* within a tumour an attractive possibility. Long wavelength absorption and high two-photon absorption cross sections are key requirements for an effective prodrug [5]. In this report we compare three related molecules (see Figure 1): combretastatin A4 and a fluorinated analogue (CA4 and CA4F, with the *Z*-isomers being highly active drugs with IC_{50} in the nanomolar region) and a 4-cyano derivative (CNCA4). Whilst *Z*-CNCA4 has relatively low toxicity (IC_{50} micromolar region), it has some photophysical properties described below that suggest a route to more effective *E*-combretastatins as photochemically active prodrugs. Our previous work has demonstrated rapid uptake and concentration of these two compounds in a range of live mammalian cells using two-photon fluorescence lifetime imaging [4,6].

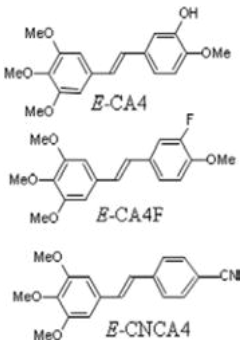

Figure 1 : Structures of E-combretastatins investigated

Fluorescence spectra of *E*-combretastatins

The fluorescence emission maximum of *E*-CNCA4 shifts to the red with increasing solvent polarity (Figure 2). Lippert plots (inset to Figure 2) show a dipole moment in the excited state of *E*-CNCA4 of 17.7 Debye, whilst that for *E*-CA4F is only 5.6 Debye. This suggests a significant transfer of electron density in the excited state of *E*-CNCA4 from the electron donating methoxy groups of the A-ring to the electron accepting 4-cyano substituent of the B-ring and formation of an intramolecular charge transfer (ICT) state. Such features are known to contribute to enhanced two-photon absorption cross sections in the near infrared [5].

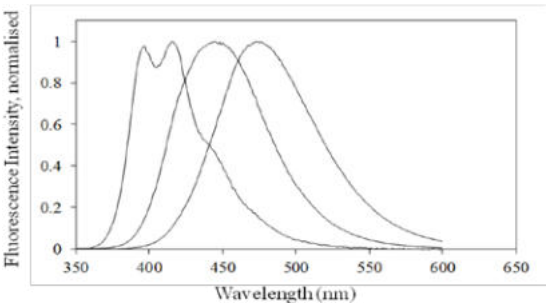

Figure 2: Fluorescence spectra of *E*-CNCA4 in cyclohexane (a), ethyl acetate (b) and dimethylsulfoxide (c). **Inset**: Lippert plots for *E*-CA4F and *E*-CNCA4

Two-photon absorption cross-sections

Figure 3 shows two-photon absorption spectra of *E*-CA4F and *E*-CNCA4 measured using the multiphoton microscope in the LSF Confocal Microscope Laboratory, using the comparative fluorescence method of Makarov et al. [7] with 9-chloroanthracene as the standard fluorophore. From the viewpoint of drug activation within tissues *E*-CNCA4 has some advantages over *E*-CA4: firstly it has a peak in the two-photon spectrum at 740 nm, whereas *E*-CA4 shows only increasing two-photon absorption below 630 nm. The longer wavelength two-photon absorption of *E*-CNCA4 avoids absorption and potentially damaging consequences of absorption by intracellular chromophores such as tryptophan [8] and extends the penetration range in tissue. Secondly, the two-photon cross section of *E*-CNCA4 at 740 nm is some 20 times higher than for *E*-CA4 at 630 nm. Consequently new drug candidates are to be based on the CNCA4 structure.

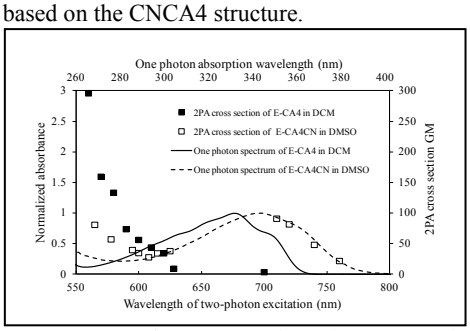

Figure 3: Two-photon (2PA) absorption cross sections (σ_2, GM units) versus wavelength overlaid with one-photon absorption spectra for *E*-CA4 (full curve) and *E*-CNCA4 (broken curve).

Time-resolved Infrared Spectroscopy of *E*-CNCA4

The features of the *E*-CNCA4 excited state were also investigated using time-resolved infrared spectroscopy using the ULTRA system. Figure 4A shows the transient absorption spectra of CNCA4 in the cyano group region after excitation at 266 nm. In chloroform the spectra show a bleaching of the ground state –CN band in the region of 2220 cm^{-1} and formation of the transient absorption at lower wavenumber consistent with weakening of the C≡N bond due to increased occupation of antibonding orbitals of the cyano group resulting from charge transfer from the methoxy groups. This intramolecular charge transfer (ICT) state follows the initial formation of the locally excited (LE) state and the initial fast process with a lifetime of 1.8 ± 0.1 ps probably represents this transformation. The ICT state subsequently decays with a lifetime of 270 ± 20 ps. In alcohols an further intermediate process is observed corresponding to a shift of the ICT band to slightly low frequency as shown in Figure 4B for ethanol. This represents the formation of a hydrogen-bonded ICT (HICT) state as demonstrated for the classical case of dimethylaminobenzonitrile [9]. The kinetics are shown in Figure 4B and indicate a lifetime of 30 ± 3 ps for formation of the HICT state in ethanol, corresponding to the rotational correlation time in liquid ethanol. Further results (not shown) indicate that in other alcohols the rate for HICT formation increases with increasing chain length range from approximately 12 ps in methanol to 80 ps in n-butanol.

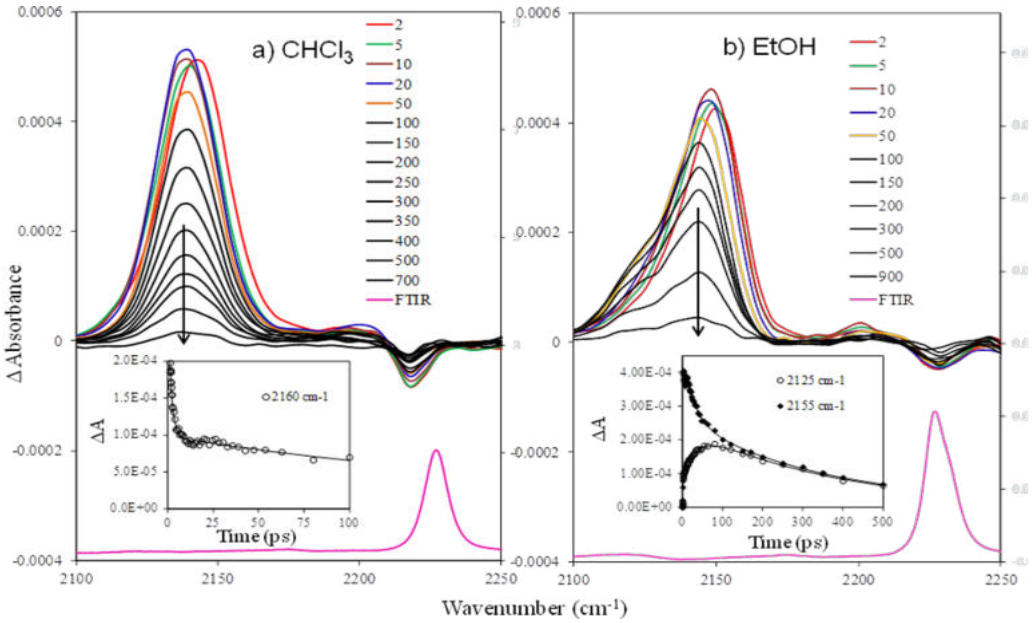

Figure 4: TRIR spectra and kinetics following excitation (266 nm) of E-CNCA4 in a) chloroform and b) ethanol.

Conclusions

The fluorescence spectra and TRIR results are strongly indicative of formation of an ICT state following excitation of *E*-CNCA4 due to electron donating and withdrawing properties of the methoxy and cyano groups respectively. In contrast the fluorescence spectra of *E*-CA4 suggest much weaker charge transfer in the excited state. This difference is reflected in the two-photon absorption spectra where *E*-CNCA4 shows a comparatively large cross section with a maximum value at about half the energy of the one-photon absorption maximum. These results suggest that further design of combretastatin-based molecules for two-photon phototherapy of vascular-dependent diseases, including many cancers, should be based on derivatives with the potential for excited states with ICT character.

Acknowledgements

We thank Mike Towrie, Ian Clark and Greg Greetham for their contributions with the TRIR experiments. At Salford we thank Alan McGown and John Hadfield for help with synthesis and discussions. We acknowledge the Biomed Network and the University of Salford for providing a studentship to KMS.

References

1. Hadfield, J.A. et al, Prog. Cell Cycle Res., 5, 309 – 325 (2003)

2. Iyer, S. et al, Cancer Res., 58, 4510-4514 (1998)

3. Lawrence, N.J. et al, Bioorg. Med. Chem. Lett., 11, 51-54 (2001)

4. Bisby, R.H. et al, Eur. J.Cancer, DOI: 10.1016/j.ejca.2011.11.025 (2011)

5. Pawlicki, M. et al, Angew. Chem. Int. Ed., 48, 3244–3266 (2009)

6. Bisby, R.H. et al, Meas. Sci. Technol., 23, 084001 (10pp). DOI:10.1088/0957-0233/23/8/084001 (2012)

7. Makarov, N.S. et al, Opt. Express,16, 4029-47 (2008)

8. Bisby, R.H. et al, Photochem. Photobiol., 85, 353-357 (2009)

9. Kwok, W.M. et al Photochem. Photobiol. Sci., 6, 987-994 (2007)

Imaging Nanoparticles in Fixed Cells using Octopus

Contact *f.j.currell@qub.ac.uk*

Fred Currell, Laura Taggart, Harold McQuaid, Mark Muir
Centre for Plasma Physics,
School of Mathematics and Physics,
Queen's University, Belfast, UK

Stan Botchway
STFC, Rutherford Appleton Laboratory, UK

Introduction

The use of nanoparticles is becoming more widespread as we experience the dawning of nanomedicine where therapeutics are delivered using nanotechnology. The main vector for delivery is gold nanoparticles, due to their biocompatibility and the ease with which they can be functionalized. Indeed a Google search reveals that about 2/3rd of publications involving functionalized nanoparticles are concerned with gold.

For example these gold nanoparticles, suitably targeted to tumours, can confer the advantages of heavy ion therapy, using far more widely available hospital Linacs [1,2]. Key to the delivery of this new type of therapy will be optimized nanoparticle preparations with good targeting properties. This targeting will also make the agents developed suitable for use as contrast agents in CT diagnosis as the gold will load the cancer cells preferentially.

Closely related to the idea of functionalization is the idea of uptake specificity, something one wishes to determine. Common approaches involve attaching a fluorescent tag to the nanoparticle and then inferring the subcellular distribution from the corresponding fluorescence signal. However the fluorescent tag can become detached so the resultant image does not report the gold distribution but instead only reports the fluorescent group's distribution. Indeed this is expected to happen as gold nanoparticles are observed to form clusters inside various cell compartments [3] suggesting their coatings are compromised by the cellular chemistry. In the approach we are investigating, the surface plasmon resonance of the gold nanoparticles is used instead. This technique is able to intrinsically detect the gold itself and furthermore it can make inferences about the degree of clumping observed.

Surface Plasmon Resonance Two Photon Excitation

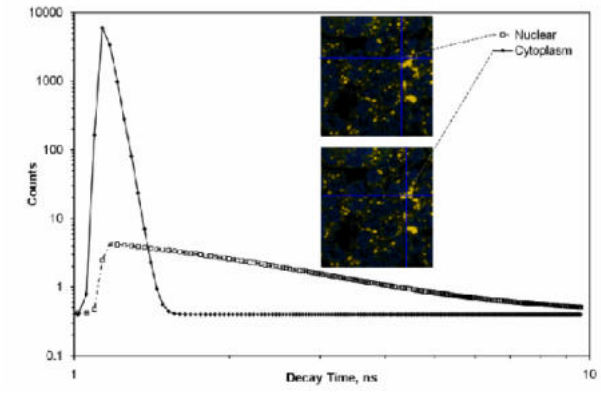

Figure 1. The surface plasmon resonance observed through multiphoton excitation with the laser tuned to 900 nm. Large aggregates of gold nanoparticles can be seen with characteristically short decay time, compared to the longer decay time of the cytoplasm.

The surface plasmon resonance is known to be wavelength dependence, being red-shifted for smaller particle size [4]. This resonance can be excited through two-photon excitation using the Octopus facility. The time signature of the resultant subsequent decay can be used to distinguish between the prompt decay due to gold and slower decay processes taking place in any surrounding biological matter (see fig.1). When the excitation laser is tuned to shorter wavelength, the distribution of smaller clumps and unclumped nanoparticles is observed (fig. 2).

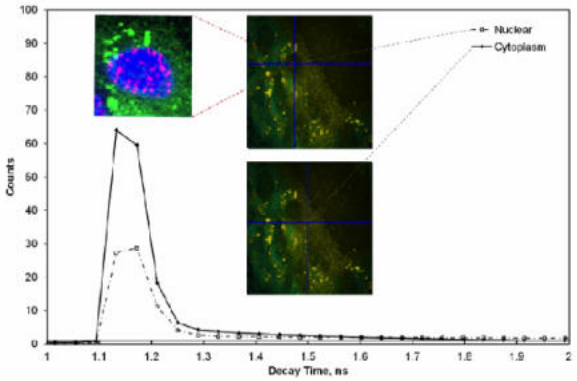

Figure 2. The surface plasmon resonance observed through multiphoton excitation with the laser tuned to 600 nm. Smaller nanoparticle aggregates are now detected both in the cytoplasm and (with much lower concentration) in the nucleus.

Sub-cellular Images and Colocalisation

Clearly this technique has great potential to infer the sub-cellular distribution of gold. Images are produced by rastering the tightly focused spot of the excitation laser across the sample whilst recording the higher energy photons produced with a photomultiplier. Furthermore, the images can be co-registered with confocal microscopy images collected using the same instrument.

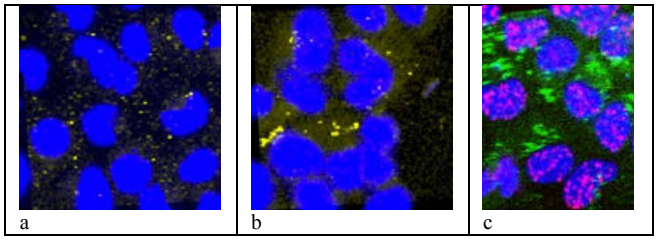

Figure 3. Examples of coregistered multiphoton and confocal images taken using MDA-MB-231 breast cancer cells, taken using 600 nm excitation under various conditions (see main text for details).

Panels a) and b) of fig. 3 show gold uptake in yellow (multiphoton signal) and the nucleus in blue (confocal image of DAPI staining). In panel a) the cells were fixed after 1 hour incubation with the gold whilst in panel b) they were fixed after 4 hours incubation. From studies of this type, using a range of nanoparticles, fixing times and cell lines a dynamical picture of gold nanoparticle uptake in cells is beginning to emerge. We plan to extend this approach to live cell imaging in the near future to further inform our knowledge of this process.

Panel c) shows gold uptake after 24 hours incubation (green) and subsequent irradiation using the Diamond light source. The γ-H2AX assay has been used to stain for DNA damage (magenta) whilst the nucleus is again stained blue. Images of this type allow us to infer the relationship between the gold uptake and the DNA radiation damage enhancement produced by the gold. Here the synergy of the proximity between Diamond and the Research Centre at Harwell allows us to study these effects using monochromatic x-rays.

Changing the x-ray photon energy changes the resultant photoelectron energy in a systematic and calculable way. Comparison of different images (like those in fig. 3c) at various photon energies leads to a biophysical model fully able to account for the observed DNA damage in terms of the transport of the photoelectron [5]. This is an example where the rich information in the co-registered confocal and multiphoton images can be used to draw clear conclusions about processes initiated by the gold on a subcellular level.

Ongoing/Future developments

As has already been discussed above, this technique allows us to learn a lot about gold nanoparticle uptake. This will be further informed by extension to live-cell imaging. Octopus has been used extensively for live-cell imaging in other contexts so the infrastructure is already in place. The major challenge will be to find a laser power able to produce the live-cell images without causing biological damage.

In spite of these ongoing challenges, as indicated in fig.4, the imaging technique will allow for much quicker evaluation of the likely benefit of a particular gold nanoparticle preparation as a dose-enhancing agent. A comparative study of the uptake of different preparations will be undertaken to demonstrate the value of the technique in this respect and additionally to develop new candidate gold nanoparticle preparations for further research. The approach will be to use the imaging as a development pipeline, replacing the conventional and much slower approach using clonogenic viability assays. The gold preparations showing the best uptake in imaging studies will then be taken through to a second phase where cell viability will be assessed. However, this step will only occur for a few preparations, after the optimization process has been completed.

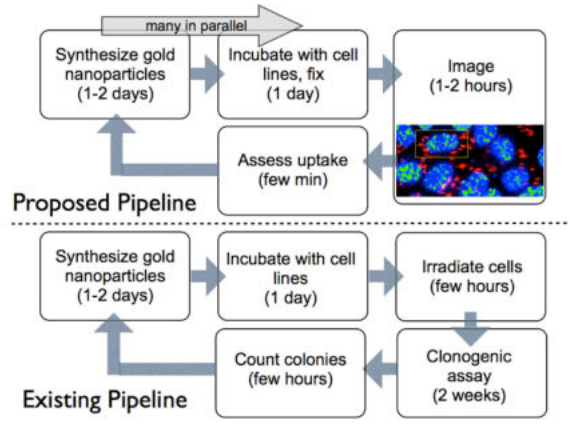

Figure 4. The proposed nanoparticle development pipeline, compared to the existing one for dose enhancing agents. Based on the hypothesis that sub-cellular uptake dictates radioenhancement, the idea is to perform initial optimization using images of gold uptake as these can be collected rapidly.

Conclusions

A powerful approach to imaging gold nanoparticles and the clusters the form in fixed cells has been described. The ability to co-register multiphoton (gold location) images with traditional confocal images has been shown. This powerful technique allows for connection of gold uptake to other endpoints that can be assessed through the use of fluorescent dyes. Future developments, including a new nanoparticle development pipeline, built on this imaging technique have been described.

Acknowledgements

We wish to thank the members of the Queen's University gold nanoparticle dose enhancement group, the staff of the Research Complex at Harwell and the staff of beamlines B16 and I15 of the Diamond Light Source who have made this research possible. We also thank the Department of Learning Northern Ireland, Cancer Research UK and the Science and Technologies Facility Council for financial support underpinning this research.

References

1. S J McMahon et al, "Biological consequences of nanoscale energy deposition near irradiated heavy atom nanoparticles" Nature Scientific Reports, **1** DOI:10.1038/srep00018 (2011)
2. S J McMahon et al, "Nanodosimetric effects of gold nanoparticles in megavoltage radiation therapy" Radiotherapy & Oncology **100** 412-416 (2011)
3. J A Coulter et al, "Cell type-dependent uptake, localization, and cytotoxicity of 1.9 nm gold nanoparticles" Intl. J. Nanomed **7**, 2673-2685 (2012)
4. P. N. Njoki et al, "Size Correlation of Optical and Spectroscopic Properties for Gold Nanoparticles" J. Phys. Chem. C **111** 14664-14669, 2007
5. F J Currell at al, *in prep* (2012)

Characterization of dynamics of protein disulphide-isomerase using single-molecule FRET

Contact *R.B.Freedman@warwick.ac.uk*

Robert Freedman and John Blood
School of Life Sciences, Gibbet Hill Campus, The University of Warwick, Coventry, CV4 7AL

David Clarke, Benjamin Coles, Christopher Tynan, Stephen Webb, and Marisa Martin-Fernandez
Central Laser Facility, Research Complex at Harwell, STFC Rutherford Appleton Laboratory, Didcot, OX11 0QX

Introduction

Protein disulphide-isomerase (PDI) is the key element of the machinery which ensures correct and efficient folding of proteins that pass through the 'export' compartments of the cell. These exported proteins include hormones, antibodies, growth factors, blood-clotting proteins etc. and many are now being developed as protein pharmaceuticals. Knowledge of the role and mechanism of action of PDI is crucial to attempts to generate more efficient cell factories for the production of such proteins (1). PDI brings about both conformational and chemical change in the proteins on which it acts, but it has been impossible to probe its mechanism in any detail because of inadequate structural and dynamic information.

PDI comprises a series of thioredoxin-like (trx-like) domains plus one inter-domain linker and a C-terminal tail (2). It is represented as a-b-b'-x-a'-c, where a and a' are highly similar redox-active trx-like domains, both with the characteristic dithiol active site sequence WCGHCK, while b and b' have the trx-like fold but without the active sites, x is a flexible linker and c is a non-essential acidic tail. The key sites are the chemical active sites in the a and a' domains and the major site for non-covalent binding of ligands, located in the b' domain.

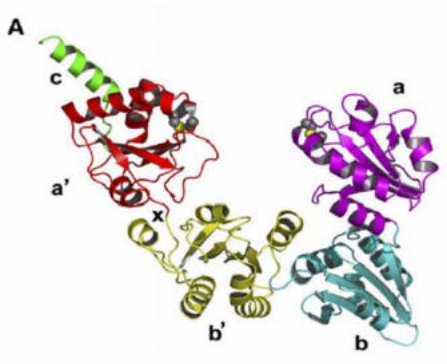

Figure 1. Structure of yeast PDI.

Evidence for flexibility and alternative conformations of PDI

PDI assists the folding of large protein substrates. An enzyme with such activity would be expected to be highly dynamic and flexible, and there is direct evidence for this. First, PDI has been abundantly available since the 1970s and yet no crystal structure has been determined for full-length mammalian PDI and structures of full-length homologues have only appeared in the past 2-3 years. This strongly suggests that the flexibility of the protein makes it very difficult to crystallize. Secondly, our studies of PDI and its fragments by intrinsic fluorescence and NMR, indicate the presence of alternative conformations (3-5).

Objective of the Work

Our overall aim is to characterise the flexibility of PDI, especially the possibility that it accesses a range of conformations, corresponding to different functional states, that differ in orientations and interactions between domains, and that it interconverts between these states in response to the binding of its functional protein partners.

Methodology

We have used single molecule fluorescence techniques available in the Lasers for Science Facility's OCTOPUS imaging cluster. Single-molecule FRET is a unique method for distinguishing the different conformers present within a population. The method was first applied to simple model systems (6) but is now proving uniquely valuable in studies on complex multi-domain proteins including chaperones (7). Human PDI has been mutated (C→A) in both active sites to give a single reactive Cys residue in each site in the sequence –WCGHAK-. The mutant protein has been expressed and purified from E.coli. in good yield, and methods have been developed for limited and specific labelling of the active-site –SH groups with N-ethyl-maleimide (NEM). A series of bifunctional maleimide reagents of different chain lengths has been reacted with the purified PDI in solution, and cross-linking of active-sites (i.e. between a and a' domains) has been analysed by SDS-PAGE. The results confirm limited earlier data (8) on bovine PDI indicating that the active sites can approach to < 2 nm. Human PDI has been labelled by simultaneous reaction with three different FRET dye pairs, selected to have different R0 values to cover the range of distances expected to be observed in PDI in its "open" and "closed" conformations (Dylight 488/Atto 665 (R0 39 Å), Atto 550/Atto 665 (R0 60Å), and Atto 550/Atto 647N (R0 65Å)). Characterization of the labelled material by solution fluorescence has indicated efficient FRET between the donor and acceptor dyes, and synchrotron radiation circular dichroism measurements on Diamond Light Source beamline B23 have confirmed that the mutated and labelled proteins are fully folded and indistinguishable from wild type PDI.

Three single molecule methods are now being used to characterize the FRET states of labelled PDI. Total internal reflection fluorescence (TIRF) is used to measure FRET in labelled PDI immobilized on glass coverslips. PDI is tagged with a streptavidin molecule at the C terminus, and this is

tethered to coverslips coated with biotin-PEG. We have used single molecule TIRF microscopy to observe individual single molecule fluorescence traces from immobilized PDI molecules. Secondly, we have also recently commissioned a TIRF-based Alternating Laser Excitation (ALEX) system in OCTOPUS. ALEX allows more complete characterization of the range of FRET states present by collecting a full set of fluorescence data (donor excitation-donor emission, donor excitation-acceptor emission, acceptor excitation-acceptor emission), and provides simultaneous information about structure and stoichiometry (9). Finally, a confocal ALEX system is in the final stages of commissioning. This will allow us to collect ALEX data from PDI in solution, and we will compare this with the TIRF data to assess the effects (if any) of immobilization on PDI conformation.

Results

Steady-state fluorescence spectroscopy has been used to characterize the dye pairs we have selected. This confirms our predictions of low, medium, and high FRET for the dye pairs (Fig. 2), so using a combination of these pairs should enable us to completely characterize the distances between PDI binding sites, from fully closed to fully open.

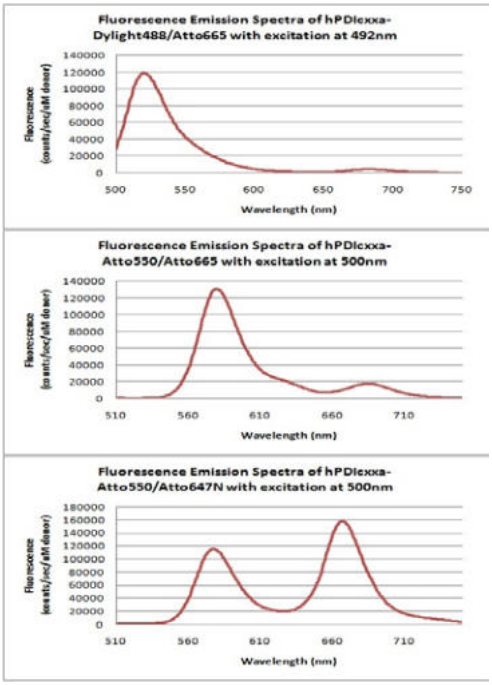

Figure 2. Steady-state fluorescence spectra for dye pairs (donor excitation). Increasing acceptor emission from top to bottom shows low, medium, and high FRET.

Preliminary *single molecule TIRF* microscopy measurements indicate the presence of at least two FRET states in PDI. Figure 3 shows example FRET traces for immobilized PDI labelled with the dye pair Atto 550/Atto 647N. The traces show step photobleaching characteristic of single molecule fluorescence. Anticorrelated traces are typical of FRET; a) and b) show a high degree of FRET, with donor fluorescence completely quenched until bleaching of the acceptor. For the FRET pair selected, this indicates a donor-acceptor distance of less than 2 nm. c) and d) show a lower degree of FRET, with partial quenching of donor fluorescence. This corresponds to a donor-acceptor distance of approximately 4-5 nm. The inset shows a typical single molecule image. There is some evidence of a conformational change during the experiment in trace d) where an anti-correlated feature shows a simultaneous increase in donor and decrease in acceptor fluorescence signal (arrowed). This suggests a transient increase in donor-acceptor distance, although many more experiments will be required to confirm this.

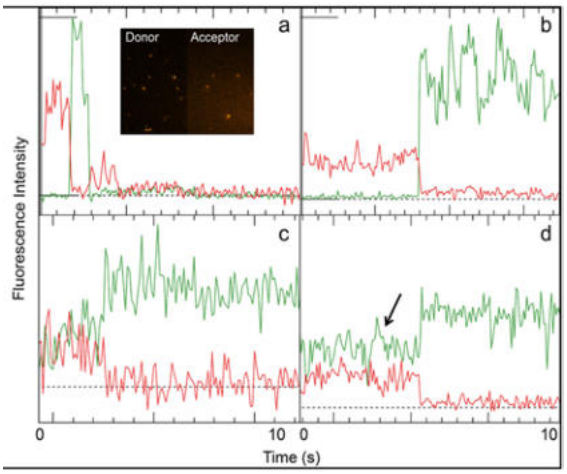

Figure 3. TIRF Single molecule fluorescence traces recorded from immobilized PDI labelled with Atto 550 and Atto 647N.

Finally, we have begun to use *TIRF ALEX* to characterize the range of distances between active sites in PDI. Figure 4 shows data from an ALEX measurement on immobilized PDI. The data indicate a range of FRET states, with a predominant species with FRET efficiency around 0.3, and a distribution of higher FRET states up to around 0.8. Further work is required, but this may correspond to fully open PDI together with a range of conformations in a more closed state.

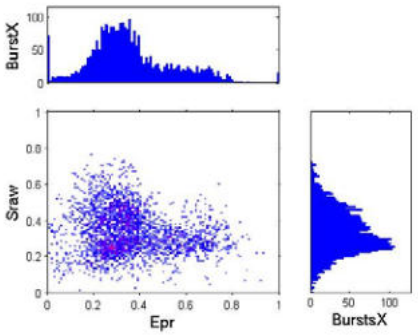

Figure 4. TIRF ALEX data from immobilized PDI labelled with Atto 550 and Atto 647N.

Next Steps

Further work is planned, to fully characterize the different conformations of PDI, and to investigate the effect of substrate binding on these conformations. We also plan to investigate PDI mutants that are thought to be constrained into open or closed conformations. Confocal ALEX will be used to check whether protein immobilization has any effect on conformation.

Acknowledgements

This work has been partially funded by the BBSRC (BB/D017807/1), and by the Wellcome Trust (16247). Studentship funding was provided by EPSRC through the Warwick MOAC Doctoral Training Centre.

References

1. Freedman, R.B. (2009) pp. 121-157 in 'Oxidative folding of peptides and proteins' eds. Buchner J. & Moroder, L. Royal Society of Chemistry. **2**. Freedman, R.B., et al. (2002) EMBO Reports 3, 136. **3**. Nguyen, V.D., et al. (2008) J. Mol. Biol. 383, 1144. **4**. Wallis, A.K., et al. (2009) Prot. Sci. 18, 2569. **5**. Byrne, L.J., et al. (2009) Biochem. J. 423, 209. **6**. Schuler, B., et al. (2002) Nature 419, 743. **7**. Mickler, M., et al. (2009) Nat. Struc. Mol. Biol. 16, 281. **8**. Hawkins, H C, et al. (1991) Biochem J. 275, 341. **9**. Santoso, Y. et al. (2008) Biochem. Soc. Trans. 36, 738.

The plant secretoryome: protein-protein interactions in the higher plant secretory pathway

Contact *chawes@brookes.ac.uk*

Chris Hawes, Imogen Sparkes, Anne Osterrieder, John Runions, Jennifer Schoberer.
Department of Biological and Molecular Sciences, Faculty of Health and Life Sciences, Oxford Brookes University, Oxford, OX3 0BP

Stanley Botchway, Andy Ward and Mark Pollard
Central Laser Facility, STFC, Rutherford Appleton Laboratory, Harwell Science & Innovation Campus, Didcot, OX11 0QX

Introduction

The Plant Cell Biology Group at Oxford Brookes University primarily researches into the structure and function of the membrane bounded organelles of the secretory pathway from the endoplasmic reticulum through to the plasma membrane.

This report summarises a continuing series of experiments looking at the use of FRET/FLIM to study protein interactions in the secretory pathway, optical tweezers to investigate Golgi-endoplasmic reticulum (ER) interactions and single molecule imaging via TIRF microscopy to investigate protein mobility in the plasma membrane.

Plant Golgi transferase interactions:

As mentioned in our previous annual report we were looking for putative interactions amongst plant Golgi-resident N-glycan processing enzymes to determine whether protein homo- and/or hetero-oligomerisation could be considered as a potential retention mechanism for integral Golgi membrane proteins and enzymes in the plant Golgi apparatus.

So far, we have focused on the full-length N-glycan processing enzymes MNS1 (Golgi α-mannosidase I), MNS3 (ER-type α-mannosidase I), GnTI (N-acetylglycosaminyltransferase I) and GMII (Golgi mannosidase II) from the *cis*- and medial-Golgi cisternae and we have found that each of the four enzymes interacts either with itself and/or at least with one of the other aforementioned enzymes.

We were finally able to test the combination GMII with itself using GFP and mRFP constructs, which so far was impossible due to low expression levels. The use of a silencing inhibitor construct remedied the problem and no reduction in the excited-state lifetime values in the GMII donor/acceptor combination was observed.

We also expressed truncations of the same aforementioned enzymes lacking the catalytic domain since it has been shown many times that the so-called CTS region comprising the cytoplasmic tail (C), the transmembrane domain (T) and the luminal stem region (S), is sufficient to target these enzymes successfully to the Golgi. To find out whether this region is actually sufficient to enable interactions that have previously been determined with full-length enzyme combinations, we tested the same set of enzymes, but with their CTS region only.

In most of the cases, similar results in terms of reduction or non-reduction of GFP excited state lifetimes could be observed for the truncated enzyme combinations. It seems that the CTS region contains sufficient or maybe the same information as their full-length counterparts in order to interact with their respective enzyme partners. This result might even indicate that the truncations are targeted to the correct Golgi sub-compartment where interaction occurs. Only the combinations MNS3-MNS1 and MNS3-GMII, respectively, did not match their full-length counterparts. In this specific case, the truncated enzyme combinations seemed to show interaction in contrast to their full-length versions. A possible explanation could be that the fluorescent proteins of the truncated enzymes reside in close proximity due to their shortened luminal C-termini (where the catalytic domain is located), whereas the fluorescent proteins of the full-length enzymes extend into the Golgi lumen much further possibly pointing away from each other and hence exceeding the 10 nm-limit required for FRET to occur.

We also investigated *cis*/medial-*trans* Golgi enzyme combinations to determine whether interactions can occur only when proteins get very close in the same or adjacent Golgi sub-compartment or whether they interact transiently or on-the-fly on their journey through the entire Golgi stack. If interactions were to occur, this could indicate a very transient and dynamic nature of protein-protein interactions in the plant Golgi apparatus. For this reason we expressed the two *trans*-Golgi enzymes GALT1 from *Arabidopsis* and ST from rat, respectively, with the *cis*-Golgi enzyme GnTI and in both cases only a little reduction in donor/acceptor lifetimes has been detected, not indicative of an occurring interaction. Co-expression with the medial-Golgi enzyme XylT (xylosyltransferase) and ST also did not result in any GFP quenching.

donor	acceptor	lifetimes (ns) mean±SD	lifetime reduction	Δ mean (ns)
GALT1		2.49±0.07		
GALT1	GnTI	2.38±0.11	4.31%	0.11
ST		2.76±0.07		
ST	GnTI	2.63±0.10	4.82%	0.13
XylT		2.45±0.06		
XylT	ST	2.43±0.07	0.93%	0.02

So far we can conclude that *cis*-Golgi located enzymes specifically interact with enzymes from the same or adjacent sub-compartments and it is not clear yet whether the same applies to late-Golgi enzymes. We will continue to investigate pairs of enzymes with distinct sub-compartmental locations in the Golgi to determine a pattern with regards to enzyme oligomerisation as a possible Golgi protein retention mechanism.

Laser tweezer applications:

During the year major advances were made with our laser trapping experiments. The experimental set up functioned far more reliably than in previous experiments which permitted us to establish a series of tests to measure trapping efficiency of plant Golgi bodies.

A) Trapping was used to investigate the role of the plant atlastin

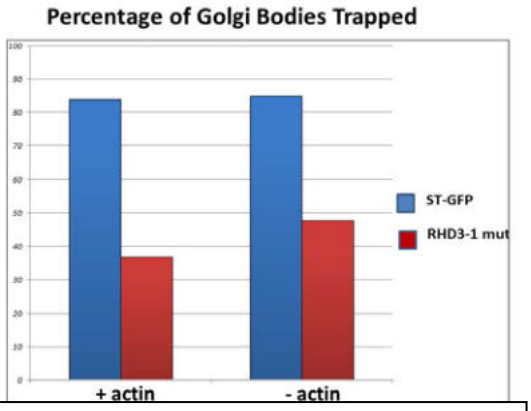

Figure 1: In mutant RHD3-1 plants the ability to trap Golgi bodies is impaired and this effect is independent of the actin cytoskeleton

homologue RHD3 in the endoplasmic reticulum (ER) membrane. Atlastin has been implicated in the fusion of ER tubules together, thus helping maintain the geometrical organisation of the ER network at the cell cortex. To do this experiment, trapping of Golgi bodies was assessed in plants expressing different RHD3 constructs, and in mutant plants by scoring the ability to trap. Also we applied a meandering trap assay to assess trapping capability at different trap speeds and laser powers. We have previously shown that when Golgi bodies are trapped and manipulated, the ER membrane remains attached to the Golgi and is stretched as the Golgi is moved. Thus Golgi movement can be used as a measure of ER tubule extension. Initial results suggest that with over expression of wild type RHD3 Golgi bodies are easier to trap than in wild type plants and with the expression of various RHD3 mutants trapping efficiency substantially declined (Figure 1). The results are interpreted as demonstrating for the first time a role in an ER protein in regulating the elasticity of the ER membrane. When mutant forms of RHD3 are expressed the ER membrane is less elastic and therefore cannot easily make three way junctions between tubules and produces more long strands of membrane. These data suggest a different role for atlastin/RHD3 than that postulated in the literature. Interestingly the presence and absence of the actin cytoskeleton made little difference to the results suggesting that the interaction of the Golgi with the ER is dominant over the Golgi/actin interaction.

B) A TIRF-based trap was used to assess the interaction of plant Golgi bodies with the actin cytoskeleton. For the first time is proved possible to trap moving Golgi and translocate individual Golgi stacks from one actin cable to another. Further work will assess the trap power required to overcome the Golgi/actin/myosin interaction.

Single molecule imaging:

In plant cell biology, the study of membrane complexity is becoming increasingly important. Plant cells have a sub-compartmentalized plasma membrane (PM) just as in yeast and animal cells. The physiological importance PM sub-structuring has been demonstrated in several studies. This topic is an open area in plant cell biology as the cell wall/PM continuum is poorly understood. Surprisingly, the relationship between membrane sub-compartmentalization and protein diffusion has not been studied in detail and only few reports have quantified protein diffusion in plant cells.

From our previous results, we know that the cell wall constrains protein lateral mobility within the PM. Cellulose microfibrils immobilise proteins inserted in the outer leaflet and constrain the diffusion of proteins in the inner leaflet of the membrane. In addition, we have some evidence showing that the cell wall has an effect on lipid packing and might increase membrane viscosity. We think that a similar model to the actin-corral system that exists in animal cells might exist in plant cells but with cellulose outside of the PM replacing the role of actin in protein sequestration. We proposed to follow the movement of molecules in living hypocotyl cells of *Arabidopsis thaliana* by TIRFM and calculate their mean square displacement over time and conclude or not whether diffusion is constrained.

By using a photoactivatable GFP fused to a PM protein LTI6b, we have been able to observe molecules at the PM surface and track them with time. Those particles are only found in transformed cell and are dependent on the cell targeting machinery. Consequently, we have been able to obtain quantitative information about the confined diffusion with the PM. Interestingly, by modifying the PM/cell wall interface with the cellulose synthesis disrupting drug Isoxaben, we were able to record a major change in the particle tracks; the mean square displacement is strongly reduced and the velocity of molecules decreased by 25%. This result confirms our previous lower resolution observations. In addition the development of single molecule tracking in plants is by itself a new approach to study protein cycling and plasma membrane sub-compartmentalization.

Acknowledgements

Some of this work was supported by a BBSRC grant to J. Runions (BB/F008147/1) and a Schrodinger Fellowship from the Austrian Government to J. Schoberer

References

1. Francin-Allami, M., Saumonneau, A., Lavenant, L., Bouder, A., Sparkes, I., Hawes, C. & Popineau, Y. (2011). Dynamic trafficking of wheat γ-gliadin and of its structural domains in tobacco cells, studied with fluorescent protein fusion proteins. Journal of Experimental Botany 62, 4507-4520.
2. Martinière, A., Lavagie, I., Nageswarana, G., Rolfe, D.J., Maneta-Peyret, L., Luu, D-T., Botchway, S.W., Webb, S.E.D., Mongrand, S., Maurel, C., Martin-Fernandez, M.L. Kleine-Vehne, J., Friml, J., Moreau, P. and Runions, J. (2012). The cell wall constrains lateral diffusion of plant plasma-membrane proteins. PNAS. In press.

Studying the role of protein dynamics coupled to light-activated enzyme catalysis using time-resolved infra-red spectroscopy.

Contact *Derren.heyes@manchester.ac.uk*

Nigel S. Scrutton

Manchester Institute of Biotechnology, University of Manchester, 131 Princess Street, Manchester M1 7DN, UK

Derren J. Heyes

Manchester Institute of Biotechnology, University of Manchester, 131 Princess Street, Manchester M1 7DN, UK

Henry J. Russell

Manchester Institute of Biotechnology, University of Manchester, 131 Princess Street, Manchester M1 7DN, UK

Alex R. Jones

Manchester Institute of Biotechnology, University of Manchester, 131 Princess Street, Manchester M1 7DN, UK

Samantha J. O. Hardman

Manchester Institute of Biotechnology, University of Manchester, 131 Princess Street, Manchester M1 7DN, UK

Greg M. Greetham

Central Laser Facility, STFC Rutherford Appleton Laboratory, Harwell Campus, Didcot, UK

Mike Towrie

Central Laser Facility, STFC Rutherford Appleton Laboratory, Harwell Campus, Didcot, UK

Introduction

Currently one of the major challenges in biology is trying to understand the physical basis of the catalytic power of enzymes. Rate enhancements of up to 10^{21} have been reported, but the physical basis of this catalytic power remains contentious (1-7). The role of protein motions/dynamics in catalysis is hotly debated but is one of the most difficult questions to address experimentally. It is now clear that enzymes are not static entities but are dynamic molecules that undergo fluctuations in structure over a range of timescales (1-7). These motions include global dynamics, involving changes in secondary structure on the nanosecond to millisecond timescale, or more local dynamics, involving the movement of protein side chains or rapid changes in local structure caused by changes in the hydrogen bonding network of solvating water molecules in a few picoseconds or less. However, how these dynamical processes are coupled to catalysis is currently one of the most important unanswered questions in enzyme catalysis. Our knowledge of enzyme motions has predominantly been gained from traditional protein crystallography and NMR techniques but these are limited in the timescales of the measurements, making it impossible to detect the rapid fluctuations in structure that may be important for catalysis. In addition, solution kinetic studies of enzyme mechanism by standard stopped-flow or laser-induced methods are limited by access to an appropriate absorbance or fluorescence signal. Much of the chemical information reporting on bond formation and breakage is spectroscopically silent, which presents a barrier to temporal resolution and detailed understanding of complex enzyme mechanisms. Our ultimate goal is to introduce a step change in our understanding of catalysis by developing a complete and quantitative picture of catalytic processes in enzyme systems driven by protein motions by using laser-induced infra-red techniques. Consequently, we have attempted to study the catalytic and dynamic processes that are associated with two enzyme systems that can be activated by light, namely the vitamin B_{12}-containing enzyme ethanolamine ammonia lyase (EAL) and protochlorophyllide oxidoreductase (POR).

Vitamin B_{12}, which is the largest of all vitamins, is a diamagnetic, six-coordinate Co^{III} complex and is the only known vitamin to contain a metal (8). The major physiologically active form is adenosylcobalamin (AdoCbl), which has an unusual covalent linkage between the cobalt and the C5' of an axial 5'-deoxyadenosyl group. AdoCbl-dependent enzymes facilitate radical rearrangement reactions in a variety of organisms (8, 9). Upon substrate binding, the unique covalent Co-C bond at the centre of AdoCbl is broken homolytically, yielding a singlet-born 5'-deoxyadenosyl and cob(II)alamin radical pair (8, 9). Remarkably, thermal homolysis rates achieved by these enzymes are ~ 10^{12} times greater than that of the free cofactor in solution (10-13). Recent data indirectly suggest protein motions may be coupled to the reaction chemistry (14). AdoCbl, in addition to its catalytic role, is a light sensitive molecule, with photoexcitation yielding a radical pair species similar to during the enzyme reaction. This has led to a number of ultrafast (fs-ns) UV-visible studies with the aim to identify structural intermediates and kinetics during enzyme turnover (15-19). We have now used time-resolved infrared (TRIR) techniques of both free and enzyme (EAL)-bound AdoCbl to provide information of structural interactions between the protein scaffold and cofactor following radical pair species formation.

POR catalyses the light-driven reduction of protochlorophyllide (Pchlide), which is a key reaction in the synthesis of chlorophyll and is important for the development of the chloroplast in plants (20, 21). The reaction has been well studied using a range of static and transient UV/vis spectroscopies leading to the elucidation of the catalytic mechanism of the enzyme. The reaction involves a light-activated hydride transfer reaction from the NADPH cofactor followed by a proton transfer step from a conserved Tyr residue in the enzyme (22). Proton transfer is reliant on an extended network of molecular motions that are slaved by solvent dynamics, whereas hydride transfer is linked only to localized motions within the enzyme's active site (23). Although the chemical steps in the POR catalytic cycle proceed on a relatively slow microsecond timescale (22), catalysis is completely reliant on picosecond excited-state processes associated with Pchlide (21). Detailed understanding of the Pchlide photochemistry has proved challenging, but over the last few years a number of time-resolved transient spectroscopy studies have identified different short-lived Pchlide* species, both in the isolated pigment and in the ternary enzyme-substrate complex (21). We have now used TRIR measurements to identify localised structural changes in the Pchlide molecule and the POR enzyme that are coupled to the active site chemistry over a range of timescales from ps to ms in order to study the entire catalytic cycle.

Materials and Methods

EAL (12) and POR (22) samples were produced as previously described. AdoCbl was purchased from Sigma and used without

further purification. Pchlide was produced as previously described (22). All samples were prepared in D_2O buffer (Goss Scientific).

Static IR Measurements

Infrared spectra were measured using a Bruker Vertex 80 spectrometer with an XSA external sample compartment. A CaF_2 transmission cell with a 100 µm path length was used, which allowed the acquisition of signals in the mid-IR region between 700–4000 cm^{-1}.

TRIR Measurements

TRIR measurements were performed at room temperature using an experimental setup described previously (24). Amplified Ti:sapphire laser pulses were used to drive optical parametric amplifiers, providing tunable visible and IR output pulses. For each experiment, the excitation beam was approximately 150 µm fwhm and set at the magic angle with respect to the IR probe beam. The sample cell used had CaF_2 windows and a 100 µm path length, and was placed in a rastering sample holder to avoid photobleaching. Changes in IR absorption were measured between 1300 and 1700 cm^{-1} by two overlapping 128 pixel detectors with a resolution of ~3 cm^{-1} per pixel.

Results and Discussion

TRIR of AdoCbl

TRIR spectra were acquired for free AdoCbl in the mid-IR from 1300-1700 cm^{-1} since this region encompasses many of the main vibrations in the cobalamin chromophore, including the corrin ring and its amide substituents. Figure 1a shows the ground state FTIR spectrum of AdoCbl, alongside the TRIR difference spectra (with the reference to the ground state) over the 2 ns following excitation at 525 nm (Figure 1b). The initial signals (from 2 ps) are those with the largest amplitudes, and represent excited state species, which then decay towards the dark state. The spectra are dominated by a bleach of the band assigned to the corrin breathing mode at around 1575 cm^{-1} (25), with an accompanying transient at 1549 cm^{-1}, and a bleach and transient at 1500 and 1470 cm^{-1}, respectively. There are peaks that shift gradually over the acquisition period: from 1337 to 1343 cm^{-1}; a peak distortion around 1485 cm^{-1}; a shift from 1549 to 1563 cm^{-1}. There are signals at 1442 cm^{-1} and 1551 cm^{-1} that initially decay more quickly (< 10 ps), shifting to higher frequencies as they do so, which we attribute to vibrational relaxation in the corrin ring. There is a very rapid peak shift in the opposite direction (to a lower frequency, from 1643 to 1628 cm^{-1}) that corresponds with the amide I region.

To extract meaningful decay rates from these spectra the TRIR data were analysed using single value decomposition (SVD), which identified two principle components (at ~ 57 and 430 ps) above noise (data not shown). The principle kinetics derived from the SVD basis spectra were globally fit to the sum of four exponentials and the calculated rate constants are given in Table 1. These data are comparable with the kinetic parameters yielded from a similar SVD analysis of the corresponding optical data from the literature (16). The excited state kinetics (k_1, k_2 and k_3) are all within an order of magnitude, although those from the TRIR data are consistently slightly faster. The difference in k_1 may be owing to vibrational relaxation, but all may be explained by the potentially different experimental conditions (room temperature etc) between the studies. The k_4 value (corresponding to radical pair recombination and cage escape) is the same within error as the UV-visible data (16).

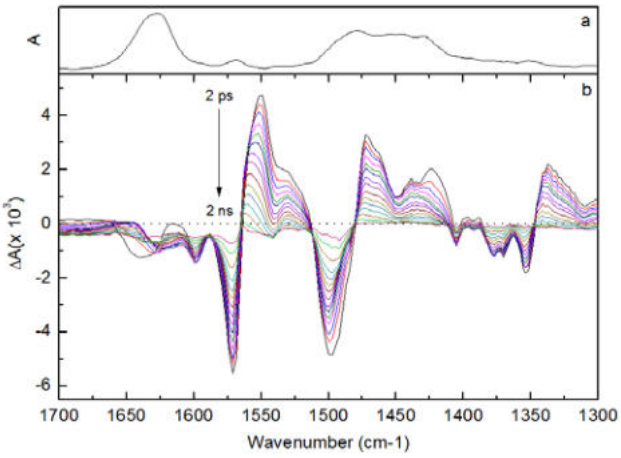

Figure 1. (a) Static FTIR spectrum of AdoCbl. **(b)** TRIR difference spectra of AdoCbl relative to the ground state from 2 ps – 2 ns. Difference spectra have been chosen to illustrate the various peak shifts over time.

Table 1. Calculated rate constants after global fitting of the principle kinetics from SVD analysis of the AdoCbl TRIR difference spectra, compared with optical ultrafast rates reported in [16].

	TRIR	UV-visible
k_1	1.73 ± 0.225 ps^{-1}	0.69 ± 0.05 ps^{-1}
k_2	0.229 ± 0.012 ps^{-1}	0.071 ± 0.001 ps^{-1}
k_3	17.5 ± 1.54 ns^{-1}	9.0 ± 1.0 ns^{-1}
k_4	2.32 ± 0.19 ns^{-1}	2.0 ± 0.2 ns^{-1}

TRIR of EAL-AdoCbl

Comparing TRIR measurements of free and EAL-bound AdoCbl provided the opportunity for us to determine whether there is interaction between the protein and cofactor following photoexcitation and Co-C bond homolysis. Selected TRIR difference spectra acquired between 1 ps – 2 ns from the EAL holoenzyme (Figure 2b) are compared to data from free AdoCbl in Figure 2c. Of particular note are the appearance of a ground state bleach at ~ 1650 cm^{-1} and a transient signal at ~ 1661 cm^{-1} in the EAL measurements, both of which coincide with the protein amide I band and decay with similar kinetics to the signal from the cofactor. There are also differences around 1425-1475 cm^{-1}, which coincide with the amide II bands of deuterated proteins (26). The lower concentration of the protein sample (~ 200 µM) compared to the free cofactor (~ 8 mM) meant that we had to average more spectra in order to acquire good quality data, and therefore collected fewer data points. Consequently, the principle kinetic from SVD analysis only fit to the sum of 2 exponentials as opposed to the 4 fit to the AdoCbl data. Although protein binding is known to affect the kinetics of AdoCbl photolysis (14, 19, 27), the most marked effect is on the excited state processes, which have not been fully resolved here. However, values for k_3 and k_4 – which represent radical pair formation and dynamics – are of the same order across the available TRIR and UV-visible data sets.

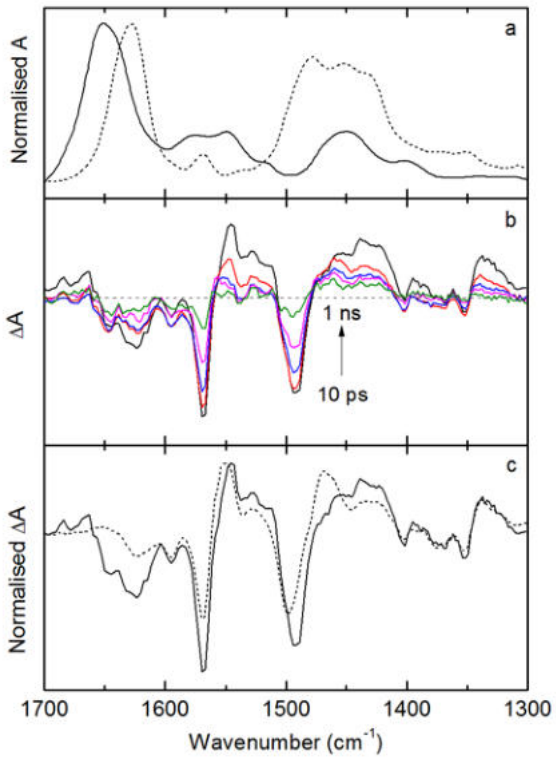

Figure 2. a) Ground state FTIR spectra of EAL holoenzyme (solid line) and AdoCbl (dashed line), normalised to peak absorbance. b) Selected TRIR difference spectra from EAL holoenzyme. c) Overlaid 10 ps TRIR difference spectra from the EAL holoenzyme (solid line) and AdoCbl (dashed line). The EAL spectrum varies in the region around 1450 cm^{-1}, a bleach at 1650 cm^{-1}, and a transient at 1661 cm^{-1}.

Ultrafast excited-state dynamics in POR

Time–resolved visible pump mid IR-probe measurements have also been used to probe the ultrafast photochemical processes required prior to hydride transfer in POR (Figure 3). Major spectral changes at ~1620 and ~1680 cm^{-1} are observed for Pchlide only and a ternary POR-Pchlide-NADPH complex. It is proposed that these spectral features represent the vibrational frequencies of the C13 keto group of Pchlide, which are likely to be coupled to structural changes to other delocalised C=C and C=N modes of the porphyrin skeleton and thought to be important for photochemistry (28). The amplitude of these spectral changes appear to be quenched in the ternary enzyme complex compared to Pchlide only (Figure 3). The quenching of these bands in the ternary complex may be explained by possible H-bonding interactions between the C13 keto and active site residues in POR (29).

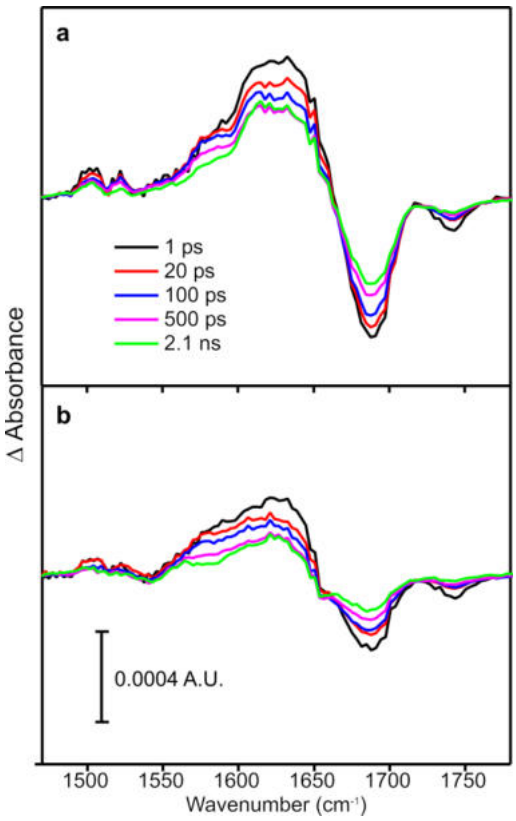

Figure 3. Time-resolved spectral changes in the mid-IR on the ps timescale for Pchlide only (a) and a POR-Pchlide-NADPH ternary complex (b) after photoexcitation at 450 nm.

IR spectral changes associated with hydride transfer in POR

The mid-IR spectral changes associated with the hydride transfer step were measured using the newly developed $TR^{M}PS$ technique (Figure 4). Samples were photoexcited with a 1 kHz ns laser pulse at 450 nm and probed using a 10 kHz fs IR laser. Several spectral features were observed after 2 µs in the ternary enzyme complex that are absent in Pchlide only samples. Some of the spectral bands are shifted when the deuterated from of NADPH (NADPD) is used, confirming they represent hydride transfer. The kinetics of the spectral changes at a number of wavelengths occur over 1-2 µs, which is the same timescale as hydride transfer (22).

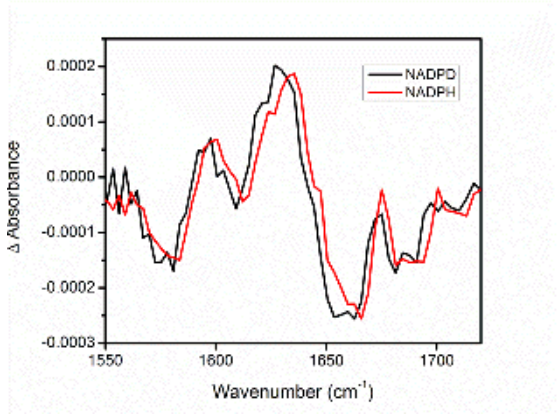

Figure 4. Time-resolved spectral changes in the mid-IR after 2 µs showing a comparison of POR-Pchlide-NADPH and POR-Pchlide-NADPD ternary complexes after photoexcitation at 450 nm.

IR spectral changes associated with proton transfer in POR

The mid-IR spectral changes associated with the proton transfer step have also been measured using the $TR^{M}PS$ technique on

the 100's µs timescale (Figure 5). Significant spectral changes after 200 µs, which are absent in Pchlide only samples, are likely to represent the formation of the chlorophyllide product. The kinetics of the spectral changes at a number of wavelengths occur on the same timescale as proton transfer (~ 200 µs) (22). We now aim to assign all of the spectral changes associated with the hydride and proton transfer chemistry by using a combination of Pchlide analogues with changes to important regions of the porphyrin molecule (30), site-directed mutants of POR, isotope labeling, cryogenic trapping data and computational approaches. By using a combination of these approaches it should be possible to assign spectral features to either the POR enzyme, Pchlide or to the NADPH cofactor.

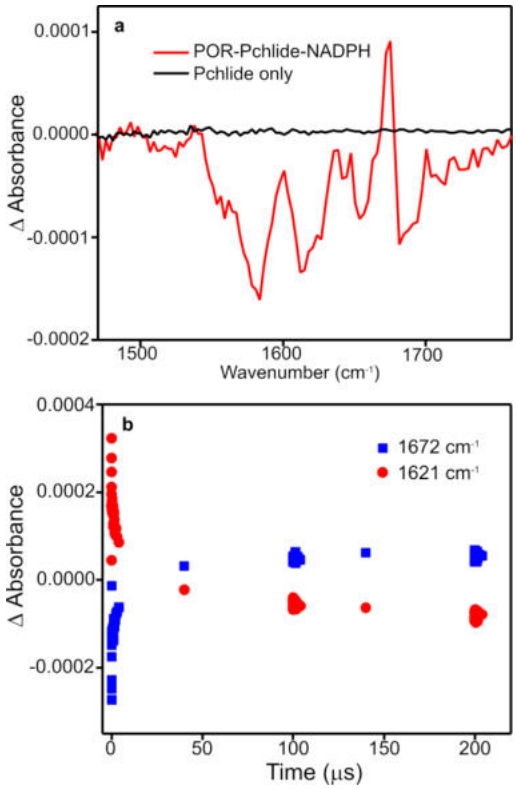

Figure 4. a). Time-resolved spectral changes in the mid-IR after 200 µs showing a comparison of Pchlide only and a POR-Pchlide-NADPH ternary complex after photoexcitation at 450 nm. **b**). Kinetics of the spectral changes at 1672 cm^{-1} and 1621 cm^{-1} for a POR-Pchlide-NADPH ternary complex over 220 µs

Conclusions

We have used laser-induced infra-red techniques to detect the rapid fluctuations in protein and chromophore structure that may be important for enzyme catalysis. We have shown that it is possible to observe IR spectral changes over a range of timescales from the fs-ms in two enzyme systems, the vitamin B_{12}-containing EAL enzyme and light-activated POR. In the future we aim to use a number of computational and experimental approaches to assign these complex spectral changes and to develop a complete and quantitative picture of catalytic processes in enzyme systems.

Acknowledgements

This work was supported by the Biotechnology and Biological Sciences Research Council (BBSRC). A.R.J. is a Colt Foundation Postdoctoral Research Fellow. N.S.S. is a Wolfson Merit Award holder and holds an Engineering and Physical Sciences Research Council (EPSRC) Established Career Fellowship. The TRIR measurements were carried out through program access support of the Science and Technology Facilities Council.

References

1. Kohen, A.; Cannio, R.; Bartolucci, S.; Klinman, J. P., Enzyme dynamics and hydrogen tunnelling in a thermophilic alcohol dehydrogenase. *Nature* **1999,** 399, 496-499.
2. Eisenmesser, E. Z.; Bosco, D. A.; Akke, M.; Kern, D., Enzyme dynamics during catalysis. *Science* **2002,** 295, 1520-1523.
3. Benkovic, S.J. ; Hammes-Schiffer, S., A perspective on enzyme catalysis. *Science* **2003,** 301, 1196-1202.
4. Garcia-Viloca, M.; Gao, J.; Karplus, M.; Truhlar, D. G., How enzymes work: analysis by modern rate theory and computer simulations. *Science* **2004,** 303, 186–195.
5. Masgrau, L.; Roujeinikova, A.; Johannissen, L. O.; Hothi, P.; Basran, J.; Ranaghan, K.E.; Mulholland, A. J.; Sutcliffe, M. J.; Scrutton, N. S.; Leys, D., Atomic description of an enzyme reaction dominated by proton tunneling. *Science* **2006,** 312, 237-241.
6. Henzler-Wildman, K.; Kern, D., Dynamic personalities of proteins. *Nature* **2007,** 450, 964-972.
7. Pisliakov, A. V.; Cao, J.; Kamerlin, S. C.; Warshel, A., Enzyme millisecond conformational dynamics do not catalyze the chemical step. *Proc. Natl. Acad. Sci. U.S.A.* **2009,** 106, 17359-17364.
8. Brown, K. L., Chemistry and enzymology of vitamin B12. *Chem. Rev.* **2005,** 105, 2075-2149.
9. Marsh, E. N.; Patterson, D. P.; Li, L., Adenosyl Radical: Reagent and Catalyst in Enzyme Reactions. *ChemBioChem* **2010,** 11, 604-621.
10. Padmakumar, R.; Banerjee, R., Evidence that cobalt-carbon bond homolysis is coupled to hydrogen atom abstraction from substrate in methylmalonyl-CoA mutase. *Biochemistry* **1997,** 36, 3713-3738.
11. Marsh, E. N.; Ballou, D. P., Coupling of cobalt-carbon bond homolysis and hydrogen atom abstraction in adenosylcobalamin-dependent glutamate mutase. *Biochemistry* **1998,** 37, 11864-72.
12. Jones, A. R.; Hay, S.; Woodward, J. R.; Scrutton, N. S., Magnetic field effect studies indicate reduced geminate recombination of the radical pair in substrate-bound adenosylcobalamin-dependent ethanolamine ammonia lyase. *J. Am. Chem. Soc.* **2007,** 129, 15718-27.
13. Hay, B. P.; Finke, R. G., Thermolysis of the Co-C Bond of Adenosylcobalamin. 2. Products, Kinetics, and Co-C Bond Dissociation Energy in Aqueous Solution. *J. Am. Chem. Soc.* **1986,** 108, 4820-4829.
14. Jones, A. R.; Hardman, S. J.; Hay, S.; Scrutton, N. S., Is There a Dynamic Protein Contribution to the Substrate Trigger in Coenzyme B12-Dependent Ethanolamine Ammonia Lyase? *Angew. Chem. Int. Ed.* **2011,** 50, 10843-10846.
15. Walker II, L. A. W.; Shiang, J. J.; Anderson, N. A.; Pullen, S. H.; Sension, R. J., Time-Resolved Spectroscopic Studies of B12 Coenzymes: The Photolysis and Geminate Recombination of Adenosylcobalamin. *J. Am. Chem. Soc.* **1998,** 120, 7286–7292.
16. Shiang, J. J.; Walker II, L. A. W.; Anderson, N. A.; Cole, A. G.; Sension, R. J., Time-Resolved Spectroscopic Studies of B12 Coenzymes: The Photolysis of Methylcobalamin Is Wavelength Dependent. *J. Phys. Chem. B* **1999,** 103, 10532-10539.

17. Yoder, L. M.; Cole, A. G.; Walker II, L. A. W.; Sension, R. J., Time-Resolved Spectroscopic Studies of B12 Coenzymes: Influence of Solvent on the Photolysis of Adenosylcobalamin. *J. Phys. Chem. B* **2001,** 105, 12180-12188.

18. Cole, A. G.; Yoder, L. M.; Shiang, J. J.; Anderson, N. A.; Walker, L. A., 2nd; Banaszak Holl, M. M.; Sension, R. J., Time-resolved spectroscopic studies of B(12) coenzymes: a comparison of the primary photolysis mechanism in methyl-, ethyl-, n-propyl-, and 5'-deoxyadenosylcobalamin. *J. Am. Chem. Soc.* **2002,** 124, 434-41.

19. Sension, R. J.; Harris, D. A.; Stickrath, A.; Cole, A. G.; Fox, C. C.; Marsh, E. N., Time-resolved measurements of the photolysis and recombination of adenosylcobalamin bound to glutamate mutase. *J. Phys. Chem. B* **2005,** 109, 18146-52.

20. Heyes, D. J.; Hunter, C. N., Making light work of enzyme catalysis: protochlorophyllide oxidoreductase. *Trends Biochem. Sci.* **2005,** 30, 642-649.

21. Scrutton, N. S.; Groot, M. L.; Heyes, D. J., Excited state dynamics and catalytic mechanism of the light-driven enzyme protochlorophyllide oxidoreductase. *Phys. Chem. Chem. Phys.* **2012,** 14, 8818-8824.

22. Heyes, D. J. ; Sakuma, M. ; De Visser, S. ; Scrutton, N. S., Nuclear quantum tunneling in the light-activated enzyme protochlorophyllide oxidoreductase. *J. Biol. Chem.* **2009,** 284, 3762-3767.

23. Heyes, D. J.; Sakuma, M.; Scrutton, N.S., Solvent-slaved protein motions accompany proton but not hydride tunneling in light-activated protochlorophyllide oxidoreductase. *Angew. Chem. Int. Ed. Engl.* **2009,** 48, 3850-3853.

24. Greetham, G. M.; Burgos, P.; Cao, Q.; Clark, I. P.; Codd, P. S.; Farrow, R. C.; George, M. W.; Kogimtzis, M.; Matousek, P.; Parker, A. W.; Pollard, M. R.; Robinson, D. A.; Xin, Z. J.; Towrie, M., ULTRA: A Unique Instrument for Time-Resolved Spectroscopy. *Appl. Spectrosc.* **2010,** 64,1311-1319.

25. Taraszka, K. S.; Chen, E.; Metzger, T.; Chance, M. R., Identification of Structural Markers for Vitamin BI2 and Other Corrinoid Derivatives in Solution Using FTIR Spectroscopy. *Biochemistry* **1991,** 30, 1222-1227.

26. Dong, A.; Hyslop, R. M.; Pringle, D. L., Differences in Conformational Dynamics of Ribonucleases A and S as Observed by Infrared Spectroscopy and Hydrogen–Deuterium Exchange. *Arch. Biochem. Biophys.* **1996,** 333, 275–281.

27. Sension, R. J.; Cole, A. G.; Harris, A. D.; Fox, C. C.; Woodbury, N. W.; Lin, S.; Marsh, E. N., Photolysis and recombination of adenosylcobalamin bound to glutamate mutase. *J. Am. Chem. Soc.* **2004,** 126, 1598-9.

28. Dietzek, B.; Kiefer, W.; Yartsev, A.; Sundstrom, V.; Schellenberg, P.; Grigaravicius, P.; Hermann, G.; Schmitt, M.; Popp, J., Protochlorophyllide a: A comprehensive photophysical picture. *ChemPhysChem* **2009,** 10, 144-150.

29. Townley, H. E.; Sessions, R. B.; Clarke, A. R.; Dafforn, T. R.; Griffiths, W. T., Protochlorophyllide oxidoreductase: A homology model examined by site-directed mutagenesis *Proteins* **2001,** 44, 329-335.

30. Klement, H.; Helfrich, M.; Oster, U.; Schoch, S.; Rudiger, W., Pigment-free NADPH:protochlorophyllide oxidoreductase from *Avena sativa L Eur. J. Biochem.* **1999,** 265, 862-874.

Human Epidermal Growth Factor Receptor (EGFR) Aligned on the Plasma Membrane Adopts Key Features of Drosophila Asymmetry

Contact *C.Tynan@stfc.ac.uk*

Chris J. Tynan
Central Laser Facility
Rutherford Appleton Laboratory

Selene K. Roberts
Central Laser Facility

Martyn Winn
CSE Department
Daresbury Laboratory

Daniel J. Rolfe
Central Laser Facility
Rutherford Appleton Laboratory

David T. Clarke
Central Laser Facility
Rutherford Appleton Laboratory

Hannes Loeffler
CSE Department
Daresbury Laboratory

Marisa Martin-Fernandez
Central Laser Facility
Rutherford Appleton Laboratory

Introduction

The human epithelial growth factor receptor (hEGFR; aka HER1) is the founding member of the growth factor receptor tyrosine kinase (RTK) super-family. This family also comprises 18 sub-groups of cell surface receptors for many growth factors, cytokines and hormones [1]. The EGFR family has evolved from one receptor/one ligand in C. elegans, through one receptor/multiple ligands in flies, to a family comprising four receptors (HER1 and ErbB2-4, known as HER2-4 in humans) and 13 extracellular ligands in mammals [2]. The EGFR family are key regulators of cell-to-cell inductive processes and cell fate [3]. Their function is to transmit growth factor signals from the outside to the inside of the cell where changes in gene expression allow the cell to respond to the new circumstances. Deregulated signalling by cell surface HER1 receptors (e.g. via activating mutations in the HER1 gene) is implicated in a substantial percentage of lung cancers [4]. As activation of these receptors has been shown to result in the growth and progression of the malignancy, there have been considerable research efforts directed toward the development of effective inhibitors of HER1. Several of these cancer drugs are in different stages of pre-clinical and clinical trials [5].

The structure of the extracellular domain of the HER1
Crystallographic studies of HER1 ectodomain fragments bound to two types of ligands, epidermal growth factor (EGF) and transforming growth factor alpha (TGFα), have shown quasi-a symmetric 2:2 ligand-receptor dimers [14, 15]. Unliganded HER1 monomers are held in a closed conformation by an intramolecular tether formed by loops in subdomains II and IV [16-18]. The data suggest that ligand binding and dimerisation involves major extracellular structural rearrangements in HER1 because in ligand-occupied receptor dimers the intramolecular tether is broken and the receptor is opened into an extended conformation which interacts with another monomer to form a back-to-back dimer [14, 15, 19].

The original paradigm proposed for the RTKs was that the ligand induced the dimerization of monomeric unliganded receptors via ligand-crosslinking of two receptor moieties [1]. Contrary to these expectations, HER1dimer structures showed that receptor dimerisation was not directly mediated by the binding of ligand but achieved exclusively via receptor-receptor contacts, suggesting a mechanism for how unliganded receptor monomers are maintained in an 'autoinhibited' configuration.

The typical representation of the holoreceptor has been derived by putting together the available crystal structures of extracellular fragments and intracellular fragments [7-9, 14-16, 19]. In this model, the extracellular domains are oriented with respect to the membrane based on the historical view that receptors are protruding from the plasma membrane as antennae.

Insights into signalling by the HER1 receptor

The primary structure of HER1 is shared by all receptor tyrosine kinases and consists of a single polypeptide chain (1,186 amino acids) of 170 kD, containing a heavily glycosylated 622-amino acid residue amino-terminal extracellular ligand binding domain that is connected to the cytoplasmic domain by a single transmembrane (TM) helix of 23 residues. The 542-residue cytoplasmic domain contains a conserved 250-amino acid tyrosine kinase core [6]. Ligand binding induces the dimerisation of HER1 ectodomains. This leads to the formation of an asymmetric dimer by the two associated intracellular kinases [7], that is stabilised by the inner juxtamembrane (JM) region [8, 9]. In the ligand-mediated kinase dimer, kinase activation proceeds though an allosteric mechanism in which the C-lobe of one kinase "pushes" the N-lobe of the other kinase towards the active site in an interaction that is highly reminiscent of the activation of CDK2 by binding of cyclinA [10]. Active kinases then proceed to phosphorylate tyrosine residues in the 229-residue carboxy-terminal tail of the receptor [7], which when posphorylated act as docking sites for a large repertoire of adapters and enzymes containing Src homology 2 (SH2) domains [11]. These include, for example Grb2, GAP, Shc, phospholipase Cγ(PLCγ), and phosphatidylinositol 3'-kinase (PI3K) , which regulate Ras/Rho-like GTPases, Ca2+ second messenger production, and the Ras-activated MAP/SAP kinase pathways [12] leading to cell proliferation, changes in cell morphology, trafficking, and the termination of signals via endocytosis of the receptor-ligand complexes [13].

Ligand-membrane distances as reporters of protein conformation

Protein conformation at the plasma membrane can be investigated from the distance from a specific site in the protein (e.g. the binding site of a cognate ligand) to the cell surface. This distance can be determined from the variation of the efficiency of Förster resonance energy transfer (FRET) between fluorescent donors labelling the protein and acceptors labelling the surface, measured as a function of acceptor surface density. FRET is a phenomenon by which the excited-state energy of an optically excited fluorescent molecule (donor) is transferred to a

neighbouring fluorescent molecule molecule (acceptor) non-radiatively via intermolecular dipole coupling [28]. FRET between donors and acceptors occurs when the electronic levels of these different molecules overlap. Being a dipole-dipole interaction, FRET is extremely sensitive to short intermolecular distances (<10 nm).

Analytical expressions describing the energy transfer process between random distributions of donors (e.g. in specific sites in proteins) and acceptors on lipid membrane surfaces have been derived for a number of geometries (see for example [28]]. The solutions to these equations are the distance of closest approach between the protein-bound fluorescent donor probe and a lipid acceptor chromophore at the plasma membrane. Examples of work using this FRET method include an investigation to derive the mean distance between the EGF binding site of HER1 and the plasma membrane of cells in suspension [29], to derive changes in conformation of α4-Integrin during activation [30], and to determine the minimum separation between the protein portion of GPI-anchored proteins to the bilayer surface [31]

HER1 aligned on the membrane adopts key features of drosophila EGFR asymmetry

To investigate the relevance of the MD-derived asymmetric model of the HER1 dimer [33] to EGF-binding heterogeneity (and/or the previously suggested negative cooperativity [26]), Tynan et al extended a FLIM -FRET assay previously reported to include FRET titrations as a function of acceptor concentration together with a data analysis method based on Monte Carlo simulations [34]. This combination allowed full quantification of the distance of closest approach between HER1-bound ligands and the surface of adherent epithelial cells, the assessment of the variation associated to the distance measurement, and also the rejection of potential sources of artifacts which can be inherent in standard flow cytometry (non-imaging) FRET measurements (e.g., photobleaching, nonradiative transfer, and nonuniform distributions of FRET donors and acceptors).

Given the known flexibility regions in the accepted crystallographic HER1 ectodomain dimer structure, the FRET-derived distance data obtained from HER1 that display high-affinity for EGF could only be reconciled with these structural data if receptors are aligned flat on the membrane (Fig. 1). MD simulations of doubly-liganded, singly-liganded and unliganded HER1 dimers aligned on a model membrane under the same conditions revealed that the asymmetry resulting from alignment on the membrane shares a number of key features with the equivalent doubly-liganded and singly-liganded structures observed recently in soluble dEGFR [27]. These results suggest that the structural basis for negative cooperativity is conserved from invertebrates to humans but that in HER1 the extracellular region asymmetry requires interactions with the plasma membrane.

Concluding remarks

FRET is commonly used at the ensemble and single molecule levels to investigate interactions between protein species (see for example [35-37]. Although less frequently employed, FRET can also be used to investigate the conformation of membrane proteins in the plasma membrane. This is derived by measuring FRET in a 2-dimensional geometry, i.e. between a plane of donor-labelled protein sites and a plane of lipid acceptors in the membrane, which allow the derivation of distances of closest approach. In cases where high-resolution structures are also available, this FRET method in combination with computational approaches (e.g. Monte Carlo simulations to derive distances of closest approach and MD simulations to relax structures in the membrane) can reveal which protein conformations are best consistent with the experimentally derived FRET-derived distances. Such an approach has very recently revealed a new conformation of HER1 in which in the ectodomain of the dimer is aligned in contact with the plasma membrane [34]. Interestingly, this conformation suggests that the structural basis for negative cooperativity is conserved from invertebrates to humans, solving a 30-year old puzzle in EGFR research.

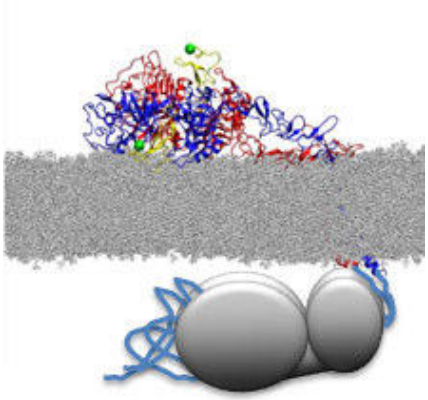

Fig. 1. Cartoon of HER1 holoreceptor combining a HER1 ectodomain dimer with two bound ligands, modelled on crystallographic structures [14-16] and placed in the membrane using MD simulations [33]. Green spheres indicate the N termini of the ligands to which donor dyes are attached. The orientation of the intracellular domain is based on electron microscopy data [39].

References

1. Schlessinger, J. (2000) Cell. 103, 211-225. **2**. Yarden, Y. and Sliwkowski, M. X. (2001) Nat Rev Mol Cell Biol. 2, 127-137. **3.** Downward, J., Parker, P. and Waterfield, M. D. (1984). Nature. 311, 483-485. **4**. Paez, J. G., et al (2004). Science. 304, 1497-1500. **5**. Jackman, D. M., et al. (2009) Clinical Cancer Research. 15, 5267-5273. **6.** Ullrich, A. et al. (1984) Nature. 309, 418-425. **7.** Zhang, X. W., Gureasko, J., Shen, K., Cole, P. A. and Kuriyan, J. (2006) Cell. 125, 1137-1149. **8**. Brewer, M. et al (2009) Mol Cell. 34, 641-651. **9** . Jura, N., et al. (2009) Cell. 137, 1293-1307. **10.** Jeffrey, P. D et al (1995) Nature. 376, 313-320. **11**. Pawson, T. (2004) Cell. 116, 191-203. **12**. Zhang, W. and Liu, H. T. (2002) Cell Research. 12, 9-18. **13**. Carpenter, G. (2000) Bioessays. 22, 697-707. **14.** Garrett, T. P. et al (2002) Cell. 110, 763-773. **15.** Ogiso, H et al (2002) Cell. 110, 775-787. **16**. Ferguson, K. M et al (2003) Mol Cell. 11, 507-517. **17.** Bouyain, S et al (2005) Proc Natl Acad Sci U S A. 102, 15024-15029. **18.** Hyun-Soo, C. and Leahy, D. J. (2002) Science. 297, 1330-1333. **19.** Burgess, A. W et al (2003) Mol Cell. 12, 541-552. **20**. Magun, B. E., et al (1980) Journal of Biological Chemistry. 255, 6373-638. 21. Shoyab, M et al (1979) Nature. 279, 387-391. **22.** Ullrich, A. et al Cell. 61, 203-212. **23.** Defize, L. H. K et al (1989) Journal of Cell Biology. 109, 2495-2507. **24.** Friedman, B. A et al (1984) PNAS. 81, 3034-3038. **25.** Mattoon, D., Klein, P., Lemmon, M. A., Lax, I. and Schlessinger, J. (2004) Proc Natl Acad Sci U S A. 101, 923-928. **26.** Macdonald, J. L. and Pike, L. J. (2008) Proc Natl Acad Sci U S A. 105, 112-117. **27.** Alvarado, D., et al (2010) Cell. 142, 568-579. **28.** Stryer, L. and Haugland, R. P. (1967) Proc Natl Acad Sci U S A. 58, 719-726. **29.** Carraway, K. L., et al (1990) Biochemistry. 29, 8741-8747. **30.** Chigaev, A., et al (2003) Biophys J. 85, 3951-3962. **31.** Lehto, M. T. and Sharom, F. J. (2002) Biochemistry. 41, 8368-8376. **32.** Webb, S. E. D et al (2008) Biophys J. 94, 808-819. **33.** Kastner, J., (2009) J Struct Biol. 167, 117-128. **34** . Tynan, C. J. (2011) Mol Cell Biol. 31, 2241-2252. **35.** Martin-Fernandez, M., et al (2002). Biophys J. 82, 2415-2427. **36.** Webb, S. E et al (2008) Opt Express. 16, 20258-20265. **37.** Webb, S. E. D. (2006) Opt. Lett. 31, 2157-2159. **38** . Wolber, P. K. and Hudson, B. S. (1979) Biophys J. 28, 197-210. **39.** van Bueren, J. J. L. et al, (2008) Proc Natl Acad Sci U S A. 105, 6109-6114

The effect of PARP inhibition on BER and B-NHEJ in the repair of simple and complex DNA damage

Contact *Pamela.Reynolds@oncology.ox.ac.uk*

P. Reynolds
Gray Institute for Radiation, Oncology & Biology, Department of Oncology, University of Oxford, Oxford, OX3 7DQ

S. L. Cooper
Gray Institute for Radiation, Oncology & Biology, Department of Oncology, University of Oxford, Oxford, OX3 7DQ

P. O'Neill
Gray Institute for Radiation, Oncology & Biology, Department of Oncology, University of Oxford, Oxford, OX3 7DQ

S. W. Botchway
Central Laser Facility, Rutherford Appleton Laboratory, Harwell Science and Innovation Campus, Didcot, OX11 0QX

A. W. Parker
Central Laser Facility, Rutherford Appleton Laboratory, Harwell Science and Innovation Campus, Didcot, OX11 0QX

Introduction

The exposure of mammalian cells to ionising radiation results in the formation of a number of DNA lesions with different complexity. The complexity of lesions induced within the DNA is related to the ionisation density of the radiation, with low linear energy transfer (LET) radiation inducing predominantly simple damage (70%) and high LET radiation inducing predominantly complex lesions (90%) (1). Previously investigations have shown that complex lesions have slower repair compared to the individual (simple) lesions (2-4).

In mammalian cells, base lesions are repaired by base excision repair (BER, Fig. 1). Recognition of the damaged base occurs by a DNA glycosylase to create an apurinic or abasic site (AP site). The DNA backbone is cleaved by an AP endonuclease creating a single stranded nick 5' to the AP site (5). It is thought that poly (ADP ribose) polymerase 1 (PARP1) may bind to the single strand gap (6). The repair can then progress through either short patch-BER (SP-BER) or long patch-BER (LP-BER) (Fig.1, (7)). In SP-BER, XRCC1 is recruited rapidly to the nick and acts as a scaffold protein for polymerase β (Pol β) and Ligase III (8). Pol β inserts the missing base and cleaves the 5' phosphate to allow ligation by Ligase III. When Pol β is unable to cleave the 5' phosphate, BER proceeds by LP-BER. During LP-BER, Pol δ or Pol ε is recruited to insert bases in a proliferating cellular nuclear antigen (PCNA) dependent manner, which results in DNA strand displacement (Fig. 1). Flap structure specific endonuclease 1 (FEN1) cleaves the DNA flap to create a ligatable structure before ligation occurs by Ligase 1 (5).

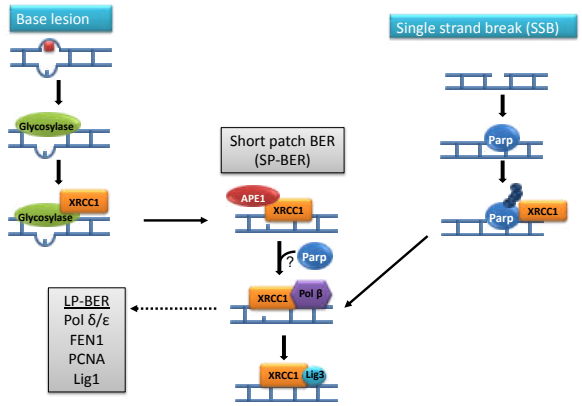

Fig. 1: Schematic diagram representing the repair of base lesions and SSBs by BER.

The most deleterious lesions induced within the DNA are double strand breaks (DSBs) and if left unrepaired, DSBs result in chromosome aberrations, mutations and ultimately cancer or cell death. Mammalian cells utilise a number of pathways to repair DSBs; classical non-homologous end joining (C-NHEJ), back-up/alternative NHEJ (B-NHEJ) and homologous recombination (HR). NHEJ is the most prevalent repair pathway, repairing DSBs throughout the cell cycle, whereas HR occurs predominantly in late S-phase early G_2-phase of the cell cycle when an intact sister chromatid is available as a template for repair. C-NHEJ involves the formation of the DNA-PK complex (Ku70/80 and DNA-PKcs) followed by the recruitment of processing factors (possibly the MRN complex, ATM, Artemis, DNA polymerase η or λ and polynucleotide kinase) before ligation occurs via XRCC4/Ligase IV/XLF (Fig. 2a). B-NHEJ has been shown to involved PARP1, XRCC1 and Ligase III (Fig 2b).

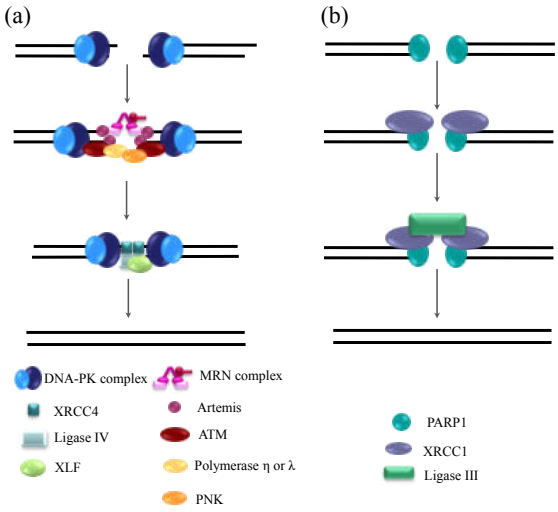

Fig. 2: Schematic diagram representing the repair of DSBs by (a) C-NHEJ (b) B-NHEJ.

Previously we have shown that NIR laser microbeam irradiation induces DNA double strand breaks of different complexity (9,10). We have investigated the role of BER in the repair of simple and complex damage by real time visualisation of XRCC1-YFP when BER is inhibited using a specific inhibitor of PARP1 activity. The kinetics of the fast component of repair involving XRCC1-YFP is unaffected compared to control cells when PARP1 activity is inhibited. The fluorescence intensity of XRCC1-YFP is significantly reduced following inhibition of PARP1. We have also initiated investigations on the contribution of B-NHEJ to the repair of DSBs and the effect on C-NHEJ. We have shown that inhibition of PARP, in C-NHEJ proficient cells, does not affect the repair kinetics involving Ku80-EGFP. Similarly the real time repair kinetics of DNA-PKcs-YFP, also involved in C-NHEJ, is unaffected by the inhibition of PARP1.

Methods

Cell culture

Ku80-EGFP tagged XRV15B ($Ku80^{-/-}$) cells were cultured in Eagles modified minimum essential medium (MEM), XRCC1-YFP tagged EMC11 ($XRCC1^{-/-}$) cells were cultured in Dulbecco's modified MEM, all medium was supplemented

with 10% foetal calf serum (FCS), 100 µg/ml penicillin streptomycin and 2 mg/ml L-glutamine at 37ºC with 5% CO_2 in air. DNA-PKcs-YFP tagged V3 (DNA-PKcs$^{-/-}$) cells were cultured in alpha modified MEM glutamax containing 10% FCS and 100 µg/ml penicillin streptomycin at 37ºC with 5% CO_2 in air.

NIR multiphoton laser set-up

A Ti:Sa laser (Mira 900, Coherent Inc., USA) tuned to 730 nm was focused through a x60 water microscope objective, numerical aperture 1.20 of an inverted microscope (TE2000, Nikon) to induce DNA damage via multiphoton excitation at the focal spot. A customised computer software programme (LabView™) operated the automated microscope stage in the x- and y-plane at a step size of 12 µm or 16 µm depending on cell type.

Real time NIR multiphoton laser microbeam irradiations

Cells were plated 24 h prior to irradiation at 2.0 x 10^5 cells per 30 mm glass bottom dish. Cells were incubated with 10 µg/ml Hoechst dye for 10 min prior to irradiation at 37°C. A red bandpass filter (RG610) was placed on top of the culture dish to prevent the Hoechst dye from absorbing UV light from ambient light. Cells were maintained at 37°C throughout the irradiation using the temperature control chamber connected to a pumped water circulator (Neslab RTE7 Digital One, Thermo Scientific). The laser was set to a wavelength of 730 nm and a nominal power of 10 mW measured through the x40 air, numerical aperture 0.95, microscope objective. Cells were irradiated in culture medium using a x60 water objective. Time 0 was recorded immediately following irradiation of the cells (less than 10 s) and images were collected at the stated times following irradiation using confocal microscopy (EC1, Nikon) equipped with an argon ion laser at 488 nm. The images were collected using three Kalman filtered scans with a minimum of 10 cells visualised for analysis per experiment.

Cells were pre-treated for 1 h with 0.1% DMSO as a control or 250 µM PARP inhibitor where applicable.

Results

Real time recruitment of XRCC1-YFP following chemical inhibition of PARP1 in cycling EMC11 cells

Cycling XRCC1-YFP tagged EMC11 cells were irradiated using the NIR multiphoton laser microbeam to visualise the recruitment and loss of XRCC1-YFP (a key component of BER) following the inhibition of PARP1 activity. The maximal XRCC1-YFP fluorescence is observed in <2 min following irradiation in dimethylsulphoxide (DMSO) control cells (Fig. 3).

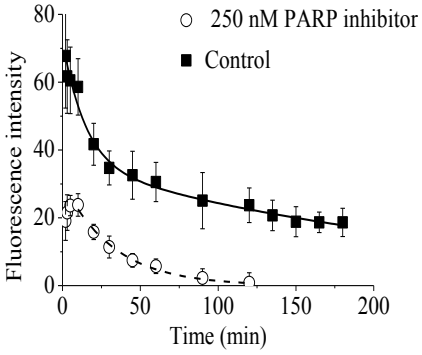

Fig. 3: Real time recruitment and loss of XRCC1-YFP fluorescence following inhibition of PARP. The graph represents the actual fluorescence intensity of XRCC1-YFP at damage sites. The inset represents the data expanded to show the first 10 min in more detail. Each point represents the fluorescence intensity of a minimum of 10 cells per experiment and the mean of 3 independent experiments ± SEM.

The actual XRCC1-YFP fluorescence intensity is 60% of the maximum at 20 min following irradiation. At 180 min, the fluorescence intensity decreases to 30% of the maximum fluorescence (Fig. 3).In PARP1 inhibitor treated cells, the maximum fluorescence is observed 5-10 min following irradiation although the maximal fluorescence is reduced compared to control cells (maximum fluorescence represents ~30% of the actual fluorescence in DMSO control cells) (Fig. 3). The fluorescence intensity decreases to 75% of the maximum fluorescence at 20 min following irradiation (Fig. 3). At 120 min, the relative fluorescence intensity is at background levels in PARP inhibitor treated cells (Fig. 3).

The repair of repair of damage, assumed to be base damage or single strand breaks (SSB), seen as the loss of XRCC1-YFP fluorescence occurs with bi-exponential decay kinetics with 54 ±16% proceeding with a $t_{1/2}$ of 8 ±4 min for the fast component and 46 ±16% proceeding with a $t_{1/2}$ of 144 ±23 min for the slow component. In PARP inhibited cells, the repair occurs by a single process with 92 ±6% proceeding with a $t_{1/2}$ of 18 ±2 min. The slower component for loss of XRCC1-YFP fluorescence is not apparent in the presence of the PAPR1 inhibitor. The loss of fluorescence intensity by the faster component in the absence of PARP1 inhibitor is similar to that seen in the presence of the inhibitor. The kinetics are similar for initial loss of fluorescence in the presence and absence of the PARP1 inhibitor.

Real time recruitment of Ku80-EGFP and DNA-PKcs-YFP following chemical inhibition of PARP1 in cycling XRV15B and V3 cells respectively

In order to determine if the XRCC1-YFP repair kinetics represent the repair of base lesions or SSBs by BER or DSBs by the B-NHEJ pathway we irradiated cycling Ku80-EGFP tagged V79B cells to visualise the recruitment and loss of the Ku80-EGFP in real time following the inhibition of PARP activity (a key component of B-NHEJ). Maximal Ku80-EGFP fluorescence intensity was observed within 1 - 2 min following irradiation in both DMSO control cells and PARP inhibitor treated cells (Fig. 4 inset). In DMSO control and PARP inhibited cells, the fluorescence decays to 65-70% of the maximum within the first 10 min (Fig. 4). At 120 min, the relative fluorescence intensity is 10% of the maximum fluorescence (Fig. 4).

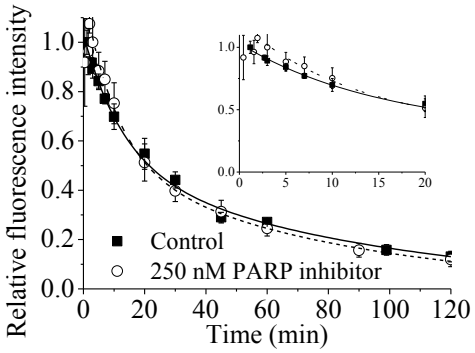

Fig. 4: Real time recruitment and loss of Ku80-EFGP fluorescence following inhibition of PARP. The inset represents the data expanded to show the first 20 min in more detail. Each point represents the normalised relative fluorescence intensity of a minimum of 10 cells per experiment and the mean of 3 independent experiments ± SEM.

Cycling DNA-PKcs-YFP tagged V3 cells were irradiated using the NIR laser microbeam to follow the recruitment and loss of the tagged protein to DNA damage in real time following the inhibition of PARP activity. Maximal DNA-PKcs-YFP fluorescence intensity was observed within 1 - 2 min following irradiation in the DMSO control and PARP inhibited cells (Fig. 5 inset). In DMSO control and PARP inhibited cells, the fluorescence decays to 50-60% of the maximum within the first

10 min (Fig. 5). At 120 min, the relative fluorescence intensity is 15-20% of the maximum fluorescence (Fig. 5).

The repair of DSBs involving Ku80-EGFP in DMSO control cells occurs with bi-exponential decay kinetics with 59 ±27% proceeding with a $t_{1/2}$ of 4 ±1 min for the fast component and 41 ±27% proceeding with a $t_{1/2}$ of 39 ±10 min for the slow component. In PARP inhibited cells, the repair occurs with bi-exponential decay kinetics 68 ±19% by $t_{1/2}$ 10 ±8 min for the fast component and 32 ±19% by 52 ±37 min for the slow component. The repair of DSBs involving DNA-PKcs-YFP occurs via a single process 63 ±28% proceeding with a $t_{1/2}$ of 37 ±28 min in control cells and 81 ±14% with a $t_{1/2}$ of 24 ±10 min following inhibition of PARP.

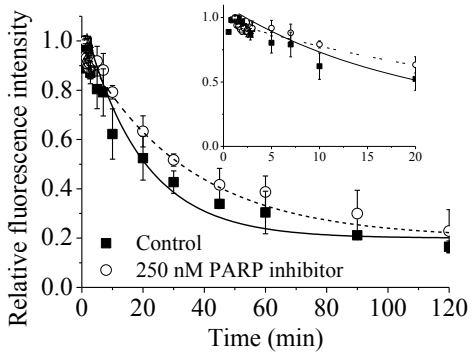

Fig. 5: Real time recruitment and loss of DNA-PKcs-YFP fluorescence following inhibition of PARP. The inset represents the data expanded to show the first 20 min in more detail. Each point represents the normalised relative fluorescence intensity of a minimum of 10 cells per experiment and the mean of 3 independent experiments ± SEM.

Conclusions

It is concluded that inhibition of the BER by a PARP1 inhibitor has little effect on the fast component of repair involving XRCC1-YFP although the slow component of repair was not observed when PARP1 activity is inhibited. XRCC1-YFP is recruited to base damage/SSBs when PARP1 activity is compromised although to a lesser extent. This is consistent with previous studies where PARP1 inhibition resulted in a loss of XRCC1 recruitment (11). This suggests that PARP is involved in the repair of DNA lesions or SSBs repaired slowly by XRCC1-YFP but may not play a significant role in the repair of the base damage/SSBs repaired via the fast component. It is proposed that the kinetics of repair involving XRCC1-YFP in C-NHEJ proficient cells represents the repair of base lesions and not DSB repair by the B-NHEJ pathway. This is based on the observation that inhibition of B-NHEJ, through inhibition of PARP, has no effect on the C-NHEJ as represented by the similar kinetics of DSB repair by Ku80-EGFP and DNA-PKcs in control and PARP inhibited cells. This is consistent with previous studies, which indicate that B-NHEJ does not significantly contribute to DSB repair when C-NHEJ is proficient (12,13).

Acknowledgements

We would like to thank CRUK and the MRC council for funding the studentship of S. Cooper. We would also like to thank Martine Lomax for discussions.

References

1. Nikjoo, H., Munson, R. J., and Bridges, B. A. (1999) *Journal of radiation research* **40 Suppl**, 85-105

2. Gulston, M., de Lara, C., Jenner, T., Davis, E., and O'Neill, P. (2004) *Nucleic Acids Res* **32**, 1602-1609

3. Leatherbarrow, E. L., Harper, J. V., Cucinotta, F. A., and O'Neill, P. (2006) *Int J Radiat Biol* **82**, 111-118

4. Botchway, S. W., Stevens, D. L., Hill, M. A., Jenner, T. J., and O'Neill, P. (1997) *Radiat Res* **148**, 317-324

5. Robertson, A. B., Klungland, A., Rognes, T., and Leiros, I. (2009) *Cell Mol Life Sci* **66**, 981-993

6. Woodhouse, B. C., and Dianov, G. L. (2008) *DNA Repair (Amst)* **7**, 1077-1086

7. Zharkov, D. O. (2008) *Cell Mol Life Sci* **65**, 1544-1565

8. Caldecott, K. W. (2003) *DNA Repair (Amst)* **2**, 955-969

9. Harper, J. V., Reynolds, P., Leatherbarrow, E. L., Botchway, S. W., Parker, A. W., and O'Neill, P. (2008) *Photochemistry and photobiology* **84**, 1506-1514

10. Botchway, S. W., Reynolds, P., Parker, A. W., and O'Neill, P. (2010) *Mutat Res* **704**, 38-44

11. Godon, C., Cordelieres, F. P., Biard, D., Giocanti, N., Megnin-Chanet, F., Hall, J., and Favaudon, V. (2008) *Nucleic acids research* **36**, 4454-4464

12. Perrault, R., Wang, H., Wang, M., Rosidi, B., and Iliakis, G. (2004) *Journal of cellular biochemistry* **92**, 781-794

13. Wang, H., Perrault, A. R., Takeda, Y., Qin, W., and Iliakis, G. (2003) *Nucleic Acids Res* **31**, 5377-5388